Algorithm Theoretical Basis for the Himawari-8, -9/AHI Cryosphere Product Part 1: Snow Cover

Yusuke YOGO*[1], Yusuke IOKA*[2], Tomonori TANIKAWA*[3]
Masahiro HOSAKA*[4], Haruma ISHIDA*[1, *5] and Teruo AOKI*[6,*3]

Abstract

Himawari-8 and -9 new-generation meteorological satellites operated by the Japan Meteorological Agency (JMA) are equipped with superior Advanced Himawari Imagers (AHIs). These optical units are vastly superior to previous versions (e.g., in terms of the number of spectral bands, spatial resolution, temporal resolution and regional rapid scanning), and support the development of a snow/ice detection algorithm. In the work reported here, the increased number of spectral bands was leveraged for the development of a new algorithm by introducing data on the Normalized Difference Water/Vegetation Indices (NDWI/NDVI), which support the identification of snow cover on vegetation. Data from full-disk observations performed at 10-minute intervals were also used to support the proposal of a new method for the combination of multiple daily snow identification results into a single outcome. The results of validation via comparison with the Automated Meteorological Data Acquisition System (AMeDAS) snow depth dataset indicated significantly better performance than that of the current product defined by a part of the cloud detection algorithm for winter over snow-covered terrain.

1. Introduction

Consisting of snow, river/lake/sea ice, glaciers and frozen soil, the cryosphere plays an important role in the climate system with its effects on the surface energy budget, hydrologic circulation, primary productivity and sea level. Climate change can be visualized in consideration of the cryosphere because of its sensitivity to temperature change (Stocker et al. 2013).

Recent years have seen a reduction in the presence of glaciers, sea ice, ice shelf content, snow and permafrost, representing a constant shrinkage of the cryosphere (Stocker et al. 2013). Increased surface air temperature causes snow and ice to melt more quickly, resulting in the exposure of low-albedo surfaces. This in turn creates higher temperatures and changes the climate system as a result of ice-albedo feedback. Against such a background, cryosphere observation and monitoring are important.

Among the various approaches to cryosphere monitoring, ground observation (such as that performed using the Automated Meteorological Data Acquisition System (AMeDAS) operated by the Japan Meteorological

*1 Satellite Application and Analysis Division, Data Processing Department, Meteorological Satellite Center
*2 Satellite Application and Analysis Division, Data Processing Department, Meteorological Satellite Center (now at Shizuoka Local Meteorological Office, Japan Meteorological Agency)
*3 Department of Physical Meteorology, Meteorological Research Institute
*4 Department of Climate and Geochemistry Research, Meteorological Research Institute
*5 Department of Observation and Data Assimilation Research, Meteorological Research Institute
*6 National Institute of Polar Research
(Received 27 December 2018, Accepted 23 April 2019)

Agency (JMA)) provides data on snow depth at more than 300 sites across Japan and yields information on discrete two-dimensional snow distribution. Geostationary meteorological satellites such as JMA's Himawari series also provide cryosphere information with high spatial and temporal resolution. Cryosphere conditions can additionally be determined in consideration of the radiative characteristics of snow and ice (e.g., Klein et al. 1998, Hall et al. 2006, Stamnes et al. 2007, Chen et al. 2014). Snow detection algorithms have been developed for past satellites (e.g., Ohkawara 1996, Uesawa 2006), and JMA's Meteorological Satellite Center (MSC) has provided a snow cover and sea ice product as a part of the Himawari-8 and -9 Cloud Mask Product (referred to here as CMP or the current product/algorithm; Imai and Yoshida 2016). As the algorithm for this product is a partly revised version of that developed for the Meteosat second generation by NWC SAF (Meteo-France 2013), there are still some issues with snow cover and sea ice product output. Thus, we can make improvements at several points to offer better products. 1) The Advanced Himawari Imager (AHI) on board Himawari-8 and -9 have high spectral, temporal and spatial resolutions. These characteristics were utilized to develop a more accurate snow cover and sea ice detection algorithm. 2) The algorithm is not fully suited to the spectral response functions of AHI bands, and generally underestimates snow cover and sea ice extent. 3) The algorithm produces misclassification in terms of snow cover on areas of vegetation. Remote sensing of such cover is challenging because vegetation reflectance spectra vary by type and season. However, very few studies have addressed this area of research (e.g., Chen et al. 2018). Against this background, two indices were incorporated into the algorithm in consideration of snow and vegetation spectral information.

In this report, Section 2 describes the features of Himawari-8 and -9, Section 3 outlines the snow detection algorithm for single scenes, Section 4 highlights the newly developed algorithm for merging multiple scenes, Section 5 presents results and related discussion, and Section 6 summarizes the content. Details of the new sea ice detection algorithm also developed are given in Part 2 of the AHI cryosphere product content (Ioka et al. 2019).

Table 1 Himawari-8 and -9/AHI specifications

Band number	Central wavelength [μm]	Spatial resolution [km]
B01	0.47	1
B02	0.51	
B03	0.64	0.5
B04	0.86	1
B05	1.6	2
B06	2.3	
B07	3.9	
B08	6.2	
B09	6.9	
B10	7.3	
B11	8.6	
B12	9.6	
B13	10.4	
B14	11.2	
B15	12.4	
B16	13.3	

2. Himawari-8/-9 and AHI

Himawari-8 and -9 are the world's first next-generation geostationary meteorological satellites (Bessho et al. 2016). They were launched on 7 October 2014 and 2 November 2016, respectively. Himawari-8 has been operational since 7 July 2015, and Himawari-9 entered backup operation service on 10 March 2017. The units took over the East Asia and Western Pacific observation previously conducted for more than three decades by five GMS (Geostationary Meteorological Satellite) units and two satellites from the MTSAT (Multi-functional Transport Satellite) series. As the technical details of Himawari-8/-9 and the AHI are described elsewhere (Bessho et al. 2016), we briefly introduce the specification of AHI in this paragraph. The imager has 16 spectral bands (see Table 1 for specifications), performing full-disk observation every 10 minutes and observation of the Japan area and specific target areas every 2.5 minutes. It can capture full-disk

imagery with a spatial resolution of up to 0.5 km.

3. Algorithm for Single Scenes

The proposed algorithm for identification of snowy areas under clear sky conditions consists of a part for single scenes and another for merging multiple scenes. This section describes the former. As shown in Figure 1, the expression involves consideration of geometrical limitations (as described in Section 3.1), desert (3.2), high-confidence cloud (3.3.1), low-confidence cloud (3.3.2) and snow detection testing (3.4), successively. It should be noted that cloud detection testing involves one stage for clouds easily distinguishable from snow cover and another for thin ice clouds that are more difficult to distinguish. Geometrical conditions and high/low-confidence cloud tests are common in sea ice detection algorithm (Ioka et al. 2019). Table 2 shows the specifications of the new snow cover product.

Table 3 shows all thresholds of the new snow detection algorithm for single scenes, with $R_{\mathrm{X.X\mu m}}$ representing solar reflectance at X.X μm and $T_{\mathrm{X.X\mu m}}$ representing brightness temperature at X.X μm.

3.1 Geometrical Conditions for Detection

This phase involves the identification of geometrically unsuited regions. The algorithm may output invalid values based on tests for the factors below.

(1) Solar Zenith Angle

The algorithm is valid only for daytime observation because observation data from the visible and near-infrared bands are needed. As the results of snow detection are unreliable with very high solar zenith angles, a threshold is set for this value.

(2) Latitude

It is assumed that tropical regions will have no snow cover. Rainforest areas may be wrongly identified as snow cover due to their high reflectance at 0.86 μm. Accordingly, low-latitude areas are ignored.

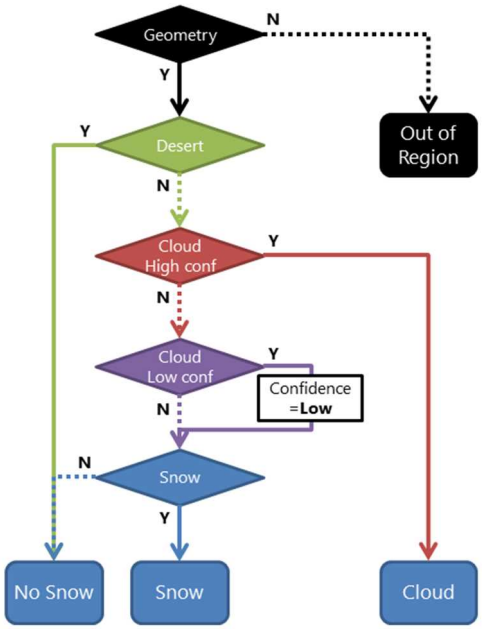

Fig. 1 Flow of the snow cover detection algorithm for single scenes

Table 2 Specifications of the new snow cover product

Region	Full disk
Spatial resolution	For each pixel of 2 km resolution HSD (Japan Meteorological Agency 2017)
Time range	24 hours (daytime analysis only)
Temporal resolution	Every 10 minutes

Table 3 Thresholds of the new snow cover detection algorithm for single scenes

Geometry		$\mathrm{SZA} < 85$ [deg] $\lvert\mathrm{Latitude}\rvert > 20$ [deg] $\mathrm{Sunglint\ Angle} > 20$ [deg]
Desert		$\frac{R_{0.86\mu m}}{R_{1.6\mu m}} > 1$
Cloud	High Conf.	$T_{3.9\mu m} - T_{10.4\mu m} < 10.0$ [K] $T_{8.6\mu m} - T_{11.2\mu m} < 0.0$ [K] $T_{7.3\mu m} > 233.15$ [K]
	Low Conf.	$T_{10.4\mu m} - T_{12.4\mu m} > 3.0$ [K] $T_{13.3\mu m} - T_{11.2\mu m} > -6.0$ [K]
Snow		$\mathrm{NDWI} > -0.94\mathrm{NDVI} + 0.29$ $\mathrm{NDWI} > 0$ $T_{10.4\mu m} < 280.15$ [K]

(3) Sunglint Angle

A geometrical condition close to specular reflection will produce higher reflectance than expected and cause misdetection. For estimation of proximity to specular reflection, the sunglint angle (also known as the cone angle) is defined as

$$\text{Sunglint Angle} \equiv \text{Arccos}\{\cos(\text{SZA})\cos(\text{VZA}) + \sin(\text{SZA})\sin(\text{VZA})\cos(\text{RAA})\}, \quad (1)$$

where SZA is the solar zenith angle, VZA is the viewing (satellite) zenith angle and RAA is the relative azimuth angle, which is the difference between the solar and viewing azimuth angles. Regions where the sunglint angle is below the threshold are ignored.

3.2 Desert Detection

(1) $R_{0.86\mu m}/R_{1.6\mu m}$

Both desert areas and water cloud regions have high reflectance at 0.86 and 1.6 μm. However, for desert areas, reflectance at 1.6 μm is higher than that at 0.86 μm, while the opposite applies for water cloud areas. The algorithm uses these characteristics to distinguish between the two. This test is run before the cloud tests.

3.3 Cloud Detection

The algorithm involves two stages of cloud detection tests. The first detects obvious clouds and labels them as "High-confidence Cloud." If any pixel has this label, the detection process will terminate. If not, the second stage is processed to detect ambiguous clouds, which are labeled as "Low-confidence Cloud." Snow cover detection is run for pixels labeled "Fine Weather (= No Clouds)" and "Low-confidence Cloud" because the latter may contain regions other than cloud, such as ocean areas with abundant water vapor. These labels are used in the multiple-scene combination process described in Section 4.

3.3.1 High-confidence Cloud Detection

Pixels returning positive test values here will be labeled as "High-confidence Cloud," and the algorithm will terminate.

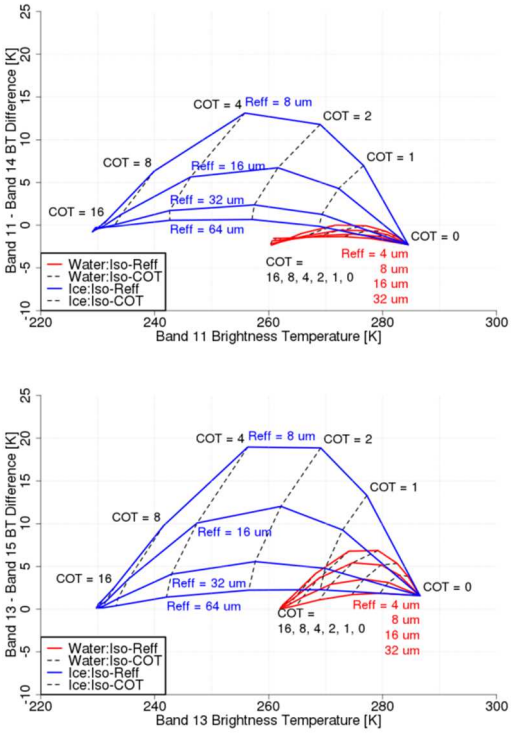

Fig. 2 Dependence between brightness temperature (BT) and brightness temperature difference at certain cloud optical thicknesses (COTs) and effective radius (R_{eff}) conditions (revised from Hayashi 2018). Red: liquid water cloud; blue: ice cloud.

(1) $T_{3.9\mu m} - T_{10.4\mu m}$

Both 3.9 and 10.4 μm radiance show equivalently high atmospheric transmittance. Using this characteristic, the solar reflection component at 3.9 μm can be estimated by subtracting $T_{10.4\mu m}$ from $T_{3.9\mu m}$. The threshold can be applied to detect water clouds, which show high reflectance at 3.9 μm.

(2) $T_{8.6\mu m} - T_{11.2\mu m}$

Generally, ice clouds are harder to distinguish from snow than liquid water clouds due to the similarity of their radiative characteristics. In ice clouds (especially those with a small effective radius), $T_{8.6\mu m} - T_{11.2\mu m}$ will be greater than 0, while areas other than ice clouds usually have values below 0 (Figure 2, top). Accordingly, $T_{8.6\mu m} - T_{11.2\mu m}$ can be used to indicate the presence of ice clouds.

(3) $T_{7.3\mu m}$

The 7.3 μm band is one of the three water vapor bands of the AHI, and responds to the lowest altitude among them. It is used to detect clouds based on water vapor absorption.

3.3.2 Low-confidence Cloud Detection

Pixels returning positive test values here will be labeled as "Low-confidence Cloud," and the algorithm will proceed to the snow detection tests.

(1) $T_{10.4\mu m} - T_{12.4\mu m}$

As shown in Figure 2 (bottom), thin clouds, regardless of water or ice status, exhibit a large brightness temperature difference between 10.4 and 12.4 μm due to their differences in emittance. However, as areas with large amounts of water vapor could show similar differences, this index results in detection of thin clouds and concentrated water vapor areas alike. Accordingly, this threshold is used for low-confidence cloud detection.

(2) $T_{13.3\mu m} - T_{11.2\mu m}$

CO_2 molecules in the atmosphere significantly affect spectral radiance at 13.3 μm, which is known as the CO_2 band. Brightness temperature at 13.3 μm is lower than that at the window band (11.2 μm) in cloud-free surface areas and low-level clouds. In high-level clouds, the CO_2 effect is small and the difference between $T_{11.2\mu m}$ and $T_{13.3\mu m}$ is also small. This test enables detection of high-level ice clouds that could be hard to distinguish from snow-covered areas.

3.4 Snow Detection

In general, snow cover and vegetation have conflicting reflective characteristics. Snow surfaces exhibit higher reflectance in visible regions and lower reflectance in near-infrared regions, while vegetation areas have the opposite characteristics. As this makes snow detection in forest areas problematic, an algorithm for this purpose was proposed.

Pixels returning positive test values here will be labeled as "Snow," and otherwise as "No Snow."

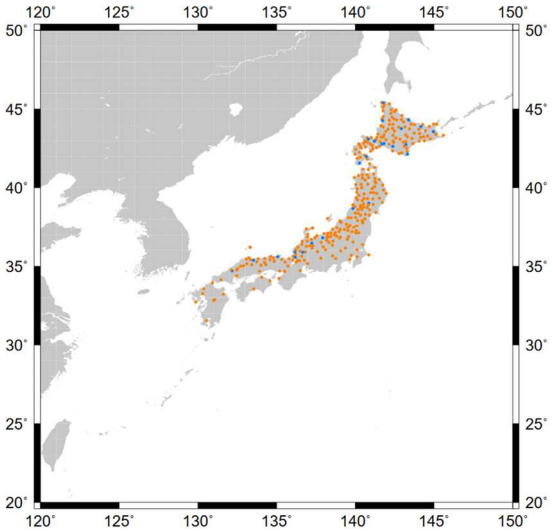

Fig. 3 AMeDAS with snow cover observation. Light blue: without sunshine observation; orange: with sunshine observation.

(1) NDWI and NDVI

This detection process involving the snow cover threshold requires satellite and ground snow observation data covering a period of several months as a minimum. In this study, data from Himawari-8 full-disk observations and AMeDAS snow depth observations (both made every 10 minutes) from 1 November 2015 to 30 April 2016 were used.

Surface observation is carried out at around 1,300 stations using automatic observation equipment under the AMeDAS framework, in which snow depth is observed at more than 300 stations in areas of heavy snowfall (Figure 3). In this study, AMeDAS snow depth data were used to determine the threshold in tests using NDWI and NDVI.

In this algorithm, NDWI is used as a snow cover index and NDVI is used as a vegetation index. The threshold defined for NDWI is loosened when NDVI is large. The threshold determination method is as follows (Figures 4 and 5):

i. Make spatial and temporal matchups between AMeDAS snow depth and AHI observation.
ii. Apply desert, high-confidence cloud and low-confidence cloud detection in the same order as the above algorithm.
iii. For points not labeled as cloud, calculate NDWI

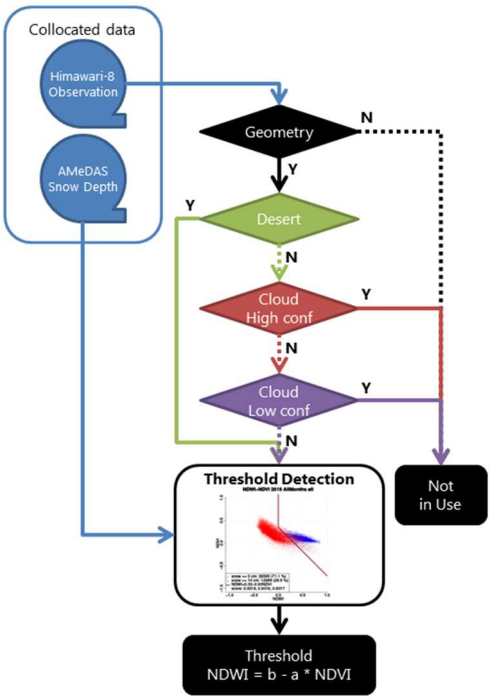

Fig. 4 Flow of threshold detection

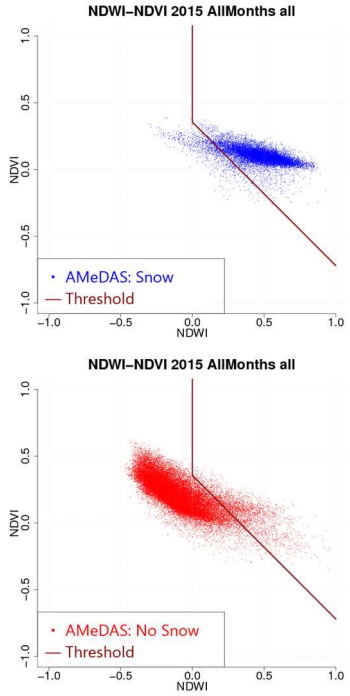

Fig. 5 Scatter plots for the relation between NDWI and NDVI. Top: snow-covered points; bottom: no-snow points.

and NDVI. Assume the thresholds in Table 3.

iv. Introduce the values of a and b in Table 3 that show the best detection score.

(2) Normalized Difference Water Index (NDWI)

If the above conditions alone were used for snow cover detection, clear areas of vegetation (characterized by high normalized difference vegetation index (NDVI) values and negative NDWI) may be misidentified as snow. Accordingly, it is assumed that areas of negative NDWI are not covered with snow based on snow reflective characteristics:

$$\mathrm{NDWI} \equiv \frac{R_{0.64\mu m} - R_{1.6\mu m}}{R_{0.64\mu m} + R_{1.6\mu m}}, \quad (2)$$

$$\mathrm{NDVI} \equiv \frac{R_{0.86\mu m} - R_{0.64\mu m}}{R_{0.86\mu m} + R_{0.64\mu m}}. \quad (3)$$

Another index involving $R_{0.51\mu m}$ and $R_{1.6\mu m}$ (the normalized difference snow index, or NDSI) is also available, but the NDWI was chosen for its superior snow detection scores.

(3) $T_{10.4\mu m}$

Removing data on very-high-temperature areas such as those of bare land with no snow cover helps to prevent misidentification of rainforest areas as snow (Hall et al. 2006).

4. Algorithm for Merging of Multiple Scenes

The algorithm enables merging of snow detection results from multiple scenes, taking all outcomes for a particular day and combining them to form a daily result. Three points should be noted regarding this procedure: 1) The current algorithm introduces merging via an OR condition (i.e., snow is considered present if one or more scenes are determined to contain snow), which could be strongly affected by misdetection for just one scene. Merging with an AND condition can be said to have the same issue. Accordingly, OR and AND conditions should be avoided. 2) Although the new algorithm has been improved in many ways, misclassification bias may be present. The merging method helps to reduce this. 3) In snow detection results for a single scene, pixels labeled as cloud are treated as equal to pixels for which snow presence/absence could not be determined due to cloud.

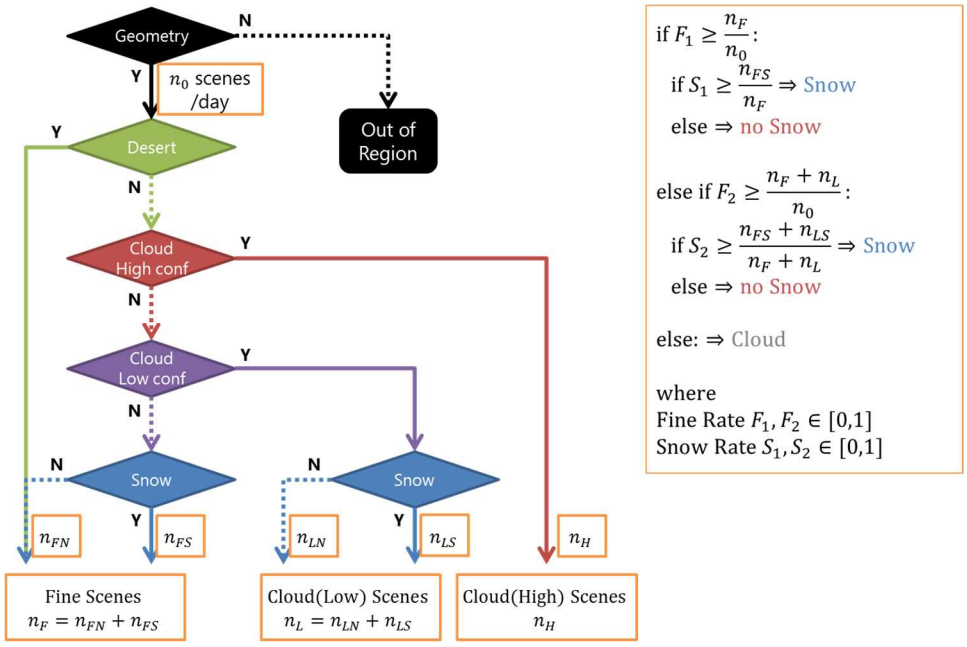

Fig. 6 Algorithm for merging of daily results. n_{XX} indicates the number of relevant scenes for the day.

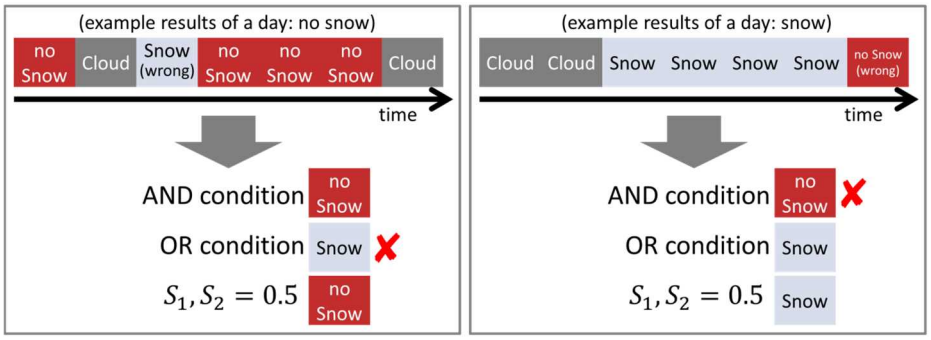

Fig. 7 Sample results for a day and combination outcomes. Left: no snow; right: snow.

The flow of the merging process is shown in Figure 6. All test processes are the same as those of the algorithm for single scenes. F_1, F_2, S_1 and S_2 are threshold values for determination of clear weather or otherwise (F_1, F_2) and snow cover or no snow cover (S_1, S_2). If large values are set for F_1 and F_2, snow detection will be more precise but the area in which detection is not possible will be bigger. If large values are set for S_1 and S_2, areas with no snow can be detected more accurately, although less so in snow-covered areas. $S_1 = S_2 = 1$ corresponds to an AND condition, and $S_1 = S_2 = 0$ corresponds to an OR condition (Figure 7). The current version involves the application of an OR condition in the merging process. If S_1 and S_2 are set appropriately, misdetection in certain scenes within a day will be mitigated and accuracy will increase.

5. Results and Discussion

The score system used is outlined here. The following equations are used to calculate the coverage ratio, OA, PA and UA:

$$\text{Coverage ratio} \equiv \frac{A+B+C+D}{A+B+C+D+E}, \quad (4)$$

$$\text{Overall accuracy (OA)} \equiv \frac{A+D}{A+B+C+D}, \quad (5)$$

$$\text{Producer's accuracy (PA)} \equiv \frac{A}{A+C}, \quad (6)$$

$$\text{User's accuracy (UA)} \equiv \frac{A}{A+B}, \quad (7)$$

where A to E are sample counts as defined in Table 4.

The coverage ratio is the ratio of scenes with content other than clouds. OA is total classification accuracy in consideration of snow-covered and non-snow-covered areas. UA refers to the probability that a pixel classified as snow by the AHI is actually in this class, whereas PA refers to the probability that snow cover will be classified as such. It should be noted here that the gap between UA and PA is considered to be a measure of under- or over-estimation in snow detection. That is, UA > PA indicates underestimation, whereas UA < PA indicates an overestimation.

First of all, as discussed in Section 4, various combinations of F_1, F_2, S_1 and S_2 can be considered. An example of this is outlined here. Figure 8 shows the coverage ratio defined by Equation (4). To maintain a high coverage ratio with high accuracy, appropriate values of F_1 and F_2 should be chosen. In this study, $F_1 = F_2 = 0.1$ from Figure 8 was set, and $S_1 = S_2 = 0.5$ was used to set the middle between OR and AND conditions.

Figures 9, 10 and 11 (left) show RGB composite imagery succinctly visualizing snow-covered areas, examples of snow detection results produced by the current algorithm and examples from the proposed new one, respectively. It should be noted that results from the current algorithm (Figure 10) are simply a by-product of CMP and are hard to validate because there is no distinction between non-snow-covered areas and clouds. It is apparent that the new algorithm allows detection of larger areas of snow cover on the Eurasian continent, and that the underestimation of the current algorithm is corrected. Figure 12 (monthly results) and Table 5 (overall averages) indicate that the new algorithm produces sufficiently accurate snow cover detection for winter (i.e., scores are all around 0.9 or more).

Table 4 Error matrix of sample counts for defining scores

Himawari \ Ground	Snow	No Snow
Snow	A	B
No Snow	C	D
Cloud	E	

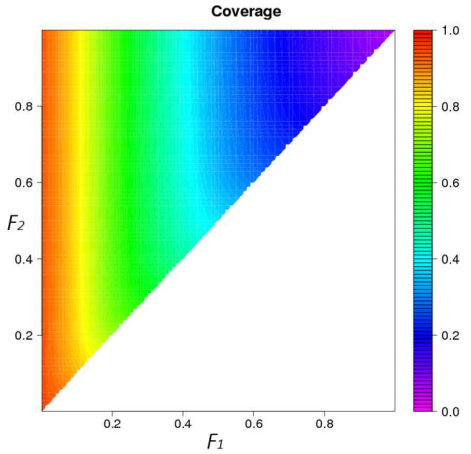

Fig. 8 Coverage ratio corresponding to F_1 and F_2.

Figure 11 shows examples of results from the single-scene algorithm and the multiple-scene merging algorithm. It can be seen that the cloud area detected using the single-scene approach is smaller with the new merging algorithm. All detection scores are also improved in comparison with single scenes (OA, PA and UA; Table 5). Figure 12 also shows that merging with an OR condition causes significant overestimation (better PA but poorer UA), while an AND condition creates significant underestimation (better UA but poorer PA). Thus, the new merging method mitigates the overestimation and underestimation observed with the single-scene method, while OR and AND conditions do not.

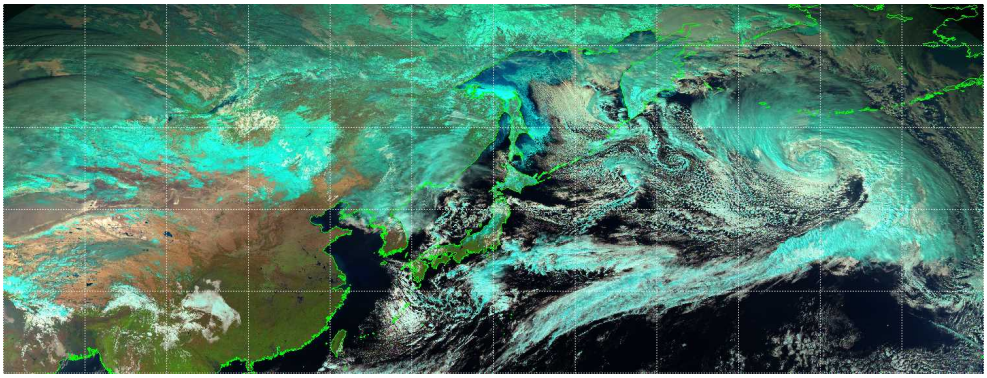

Fig. 9 Himawari-8/AHI natural color RGB image for 03:00 UTC on 08 Feb 2016.
Cyan indicates ice clouds, snow-covered areas and sea ice.

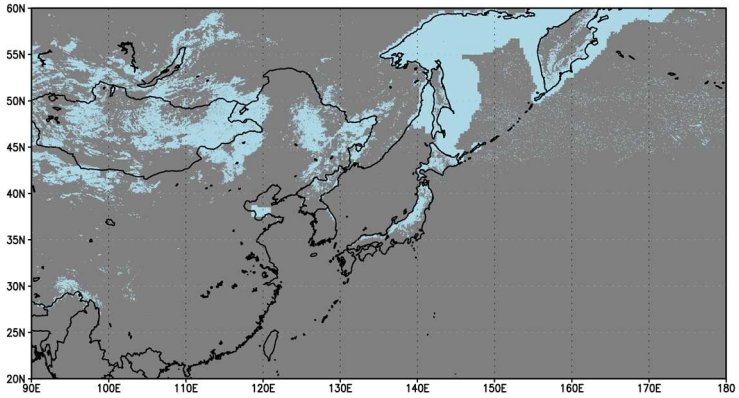

Fig. 10 Snow detection results from the previous algorithm (multi-day merging until 08 Feb. 2016).
Light blue: snow/sea ice; grey: not applicable.

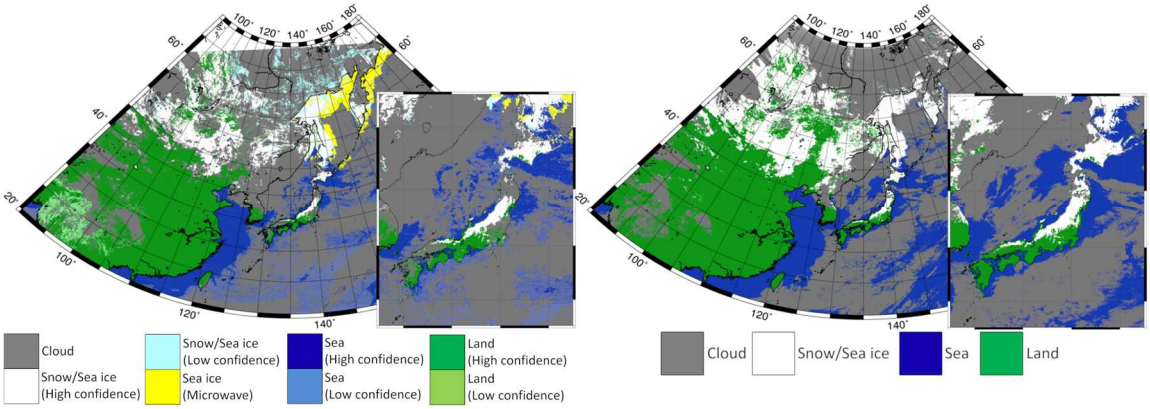

Fig. 11 Snow detection results from the new algorithm.
Left: single scene (08 Feb. 2016, 0300 UTC); right: one-day merge (08 Feb. 2016).

Table 5 Snow detection scores with the new algorithm, single-scene and 1-day merge (averaged for the period Nov. 2015 – Apr. 2017).

	Single scene	1-day merge $F_1 = F_2 = 0.1$ OR condition	1-day merge $F_1 = F_2 = 0.1$ AND condition	1-day merge $F_1 = F_2 = 0.1$ $S_1 = S_2 = 0.5$
Overall Accuracy	0.924	0.764	0.877	0.947
Producer's Accuracy	0.928	0.981	0.613	0.931
User's Accuracy	0.889	0.567	0.979	0.901

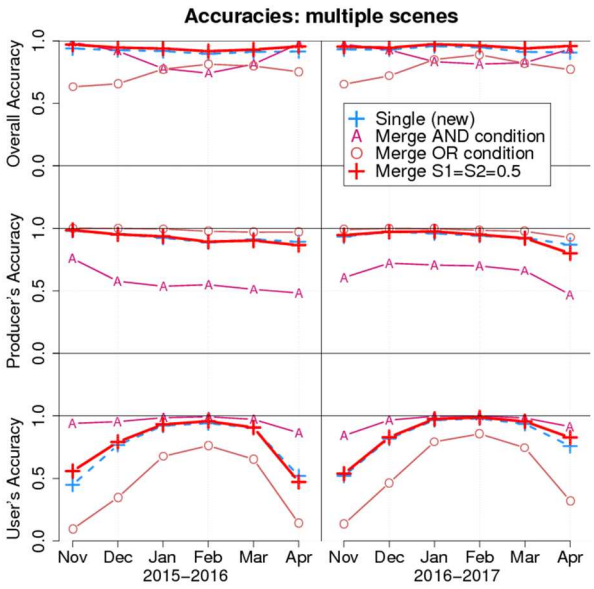

Fig. 12 Monthly snow detection scores from the new algorithm compared with AMeDAS from Nov. 2015 to Apr. 2017

6. Summary

The new optical imagers AHI for the new generation meteorological satellites Himawari-8 and -9 have been improved in terms of their spectral, temporal and spatial resolution. In this study, a new snow detection method was proposed to fully leverage the features of these units. The approach involves: 1) new thresholds for single scenes based on the utilization of new spectral bands (e.g., NDWI and NDVI) for more accurate detection of clouds and snow cover, and 2) a merging method that comprehensively leverages full-disk observations conducted every 10 minutes and combines multiple daily outcomes into a more accurate single daily result. Application of the method results in identification of greater snow cover extents and significantly higher values for all scores (OA, PA and UA), and can therefore be considered to improve snow detection accuracy.

Acknowledgement

The authors are grateful to Dr. Masashi Fukabori for his helpful and constructive comments.

References

Bessho, K., K. Date, M. Hayashi, A. Ikeda, T. Imai, H. Inoue, Y. Kumagai, T. Miyakawa, H. Murata, T. Ohno, A. Okuyama, R. Oyama, Y. Sasaki, Y. Shimazu, K. Shimoji, Y. Sumida, M. Suzuki, H. Taniguchi, H. Tsuchiyama, D. Uesawa, H. Yokota, and R. Yoshida, 2016: An introduction to Himawari-8/9 — Japan's new-generation geostationary meteorological satellites. *J. Meteor. Soc. Japan*, **94**, 151-183.

Chen, N., W. Li, T. Tanikawa, M. Hori, T. Aoki, K. Stamnes, 2014: Cloud mask over snow/ice covered areas for the GCOM-C1/SGLI cryosphere mission: validations over Greenland. *J. Geophys. Res.: Atmos*, **119**, 12287-12300. doi: 10.1002/2014JD022017

Chen, N., W. Li, C. Gatebe, T. Tanikawa, M. Hori, R. Shimada, T. Aoki and K. Stamnes, 2018: New neural network cloud mask algorithm based on radiative transfer simulations. *Remote Sens. Environ.*, **219**, 62-71.

Hall, D. K., G. A. Riggs and V. V. Salomonson, 2006: "MODIS Snow and Sea Ice Products," in Earth Science Satellite Remote Sensing - Volume I: Science and Instruments, J.J. Qu, W. Gao, M. Kafatos, R.E. Murphy and V.V. Salomonson (eds.), Springer, New York, 154-181.

Hayashi, M., 2018: Introduction to the Computation Method for Cloud Radiative Processes and Its Application for the Advanced Himawari Imager onboard Himawari-8. *Meteorological Satellite Center Technical Note*, **63**. (in Japanese with English abstract)

Imai, T. and R. Yoshida, 2016: Algorithm Theoretical Basis for Himawari-8 Cloud Mask Product. *Meteorological Satellite Center Technical Note*, **61**, 1-16.

Ioka, Y., Y. Yogo, T. Tanikawa, M. Hosaka, H. Ishida and T. Aoki, 2019: Algorithm Theoretical Basis for the Himawari-8, -9/AHI Cryosphere Product Part 2: Sea Ice Distribution. *Meteorological Satellite Center Technical Note*, **64**, 13-21.

Japan Meteorological Agency, 2017: Himawari-8/9 Himawari Standard Data User's Guide. Available on http://www.data.jma.go.jp/mscweb/en/himawari89/sp

ace_segment/sample_hisd.html

Klein, A. G., D. K. Hall, and G. A. Riggs, 1998: Improving snow cover mapping in forests through the use of a canopy reflectance model. *Hydrol. Process.*, **12**, 1723-1744. doi: 10.1002/(SICI)1099-1085(199808/09)12:10/11<1723::AID-HYP691>3.0.CO;2-2

Meteo-France, 2013: Algorithm Theoretical Basis Document for "Cloud Products." 87 pp. http://www.nwcsaf.org/AemetWebContents/ScientificDocumentation/Documentation/MSG/SAF-NWC-CDOP2-MFL-SCI-ATBD-01_v3.2.1.pdf

Ohkawara, N., 1996: Snow-ice Index. *Meteorological Satellite Center Technical Note*, Special Edition, 115-117. (in Japanese with English abstract)

Stamnes, K., W. Li, H. Eide, T. Aoki, M. Hori, and R. Storvold, 2007: ADEOS-II/GLI snow/ice products: Part I—Scientific basis. *Remote Sens. Environ.*, **111**, 258–273. doi: 10.1016/j.rse.2007.03.023

Stocker, T. F., D. Qin, G.-K. Plattner, L. V. Alexander, S. K. Allen, N. L. Bindoff, F.-M. Breon, J. A. Church, U. Cubasch, S. Emori, P. Forster, P. Friedlingstein, N. Gillett, J. M. Gregory, D. L. Hartmann, E. Jansen, B. Kirtman, R. Knutti, K. Krishna Kumar, P. Lemke, J. Marotzke, V. Masson-Delmotte, G. A. Meehl, I. I. Mokhov, S. Piao, V. Ramaswamy, D. Randall, M. Rhein, M. Rojas, C. Sabine, D. Shindell, L. D. Talley, D. G. Vaughan and S.- P. Xie, 2013: Technical Summary. In: Climate Change 2013: The Physical Science Basis. Contribution of Working Group I to the Fifth Assessment Report of the Intergovernmental Panel on Climate Change [Stocker, T. F., D. Qin, G.-K. Plattner, M. Tignor, S. K. Allen, J. Boschung, A. Nauels, Y. Xia, V. Bex and P. M. Midgley (eds.)]. Cambridge University Press, Cambridge, United Kingdom and New York, NY, USA.

Uesawa, D., 2006: Snow-Ice Index. *Meteorological Satellite Center Technical Note*, Special Edition, 125-128. (in Japanese with English abstract)

ひまわり８・９号による雪氷域検出プロダクト その１：積雪域

余郷友祐*1、井岡佑介*2、谷川朋範*3、保坂征宏*4、石田春磨*1, *5、青木輝夫*6,*3

要旨

気象庁が運用する新世代静止気象衛星ひまわり 8・9 号は、従来よりも観測波長帯の増加、時間・空間分解能の向上、高頻度領域観測の拡充といった面で大きな進化を遂げた可視赤外放射計 Advanced Himawari Imager (AHI)を搭載している。この観測性能の向上により、追加された観測波長帯を用いた新条件式や、高頻度観測を活用するための複数シーン結合処理の導入など、多くの場面でその機能を活用した雪氷域検出アルゴリズムの改良を施すことができ、それによる雪氷域検出精度の向上が見込まれる。本報告では、ひまわり 8・9 号/AHI の機能を活用して改良を行った雪氷域検出アルゴリズムのうち、積雪域検出部分についての概要と、地上観測と比較した精度検証の結果を示した。今回積雪域検出の精度を AMeDAS 積雪深データと比較して算出したところ、正答率 90%を超える極めて高い精度を実現できることが分かった。

*1 気象衛星センターデータ処理部解析課
*2 気象衛星センターデータ処理部解析課（現：気象庁静岡地方気象台）
*3 気象研究所気象予報研究部
*4 気象研究所気候・環境研究部
*5 気象研究所気象観測研究部
*6 国立極地研究所
(2018 年 12 月 27 日受領、2019 年 4 月 23 日受理)